Extreme Mechanics Letters 55 (2022) 101823

Contents lists available at ScienceDirect

Extreme Mechanics Letters

journal homepage: www.elsevier.com/locate/eml

Capillary coalescence of two partially immersed slender structures

Emmanuel Siéfert, Hoa-Ai Béatrice Hua, Fabian Brau *

Université Libre de Bruxelles (ULB), Nonlinear Physical Chemistry Unit, CP231, 1050 Bruxelles, Belgium

ARTICLE INFO

Article history:
Received 8 April 2022
Received in revised form 13 June 2022
Accepted 14 June 2022
Available online 18 June 2022

Keywords:
Capillarity
Elasticity
Coalescence
Subcritical bifurcation

ABSTRACT

We study the onset of coalescence between two slender structures quasi-statically withdrawn from a liquid bath. When partially immersed, they interact with each other through the capillary force induced by their menisci. As they are removed from the bath, their dry length increases and they become easier to bend until the capillary force is strong enough to trigger contact. Surprisingly, the structures snap to contact from a finite distance at a critical dry length. The transition to coalescence is thus subcritical and exhibits a large hysteresis loop between two stable states. An analytical coalescence criterion is derived and agrees well with experimental data for rods and lamellae. This simple elastocapillary model is a first step to better understand the elastocapillary coalescence of slender structures in fluid capture systems.

1. Introduction

The aggregation of elastic structures by capillary forces is a common phenomenon in both natural and man-made systems [1,2]. It can be observed when wet hairs [3–5] or tarsal setae of arthropods [6,7] aggregate into bundles, during nectar feeding by some small animals [8–11] or during the spontaneous in-drop spooling of spider capture thread [12], to name a few. In technology, the capillary attraction between slender structures may lead to disastrous damages in photo-resist lithography [13–16]. Recently, this capillary attraction has been used to develop complex self-assembling structures, such as helical clusters of nanopillars, at scales where conventional manufacturing strategies are hardly applicable [17–21]. Although the configuration where the free ends of the structures are in contact has been well characterized [3–5], as well as the evaporation effect on aggregation [22,23] or the imbibition and fluid transport dynamics in those structures [24–26], the necessary conditions for the coalescence of slender structures withdrawn from a liquid bath are not known to the best of our knowledge.

To study the onset of capillary aggregation of slender structures, we consider a model system composed of pairs of identical rods or lamellae quasi-statically withdrawn from a liquid bath and analyze under which conditions they coalesce (Fig. 1(a)). The presence of the structures indeed distorts the air–liquid interface resulting in an attractive capillary-induced interaction between both structures (Fig. 1(d)). Such a mechanism is reminiscent of the capillary interaction between particles at an air–liquid interface, known as the "Cheerios effect", that has been at the core of many experimental and theoretical studies [27–36] and used to program particle self-assembly [37,38]. This attractive shear force leads to the deflection of the structures towards each other and to a smaller separation distance, that in turn increases the amplitude of the shear force. In this work, we aim at describing and rationalizing the nonlinear fluid–structure coupling in this model experiment. This study is a first step to better understand the physics at play when a brush is removed from a paint bucket [39–41] or in the feeding process of some nectarivores characterized by brush-like tongues, such as bees [11,42] or bats [43].

The paper is organized as follow. In Section 2, the experimental setup is described and the results are presented. We show that the coalescence between the structures occurs through a snapping transition when they are still at a finite distance from each other and weakly deformed. In Section 3, we introduce a theoretical model to rationalize the observations based on the linear beam equation and the capillary shear force for rods and lamellae acting as a boundary condition on the beam. This nonlinear coupling reveals a subcritical bifurcation, in agreement with observations, that depends on dimensionless combinations of the system parameters. Despite the simplifying assumptions, the model allows the construction of phase diagrams that accurately describe our experimental data over a wide range of parameters. We finally summarize our work and propose some directions for future work in Section 4.

2. Experiments and results

2.1. Experimental methods

A pair of identical rods and lamellae are clamped vertically to a linear stage (ZwickiLine Z0.5 from Zwick), at a relative

* Corresponding author.
E-mail address: fabian.brau@ulb.be (F. Brau).

https://doi.org/10.1016/j.eml.2022.101823
2352-4316/

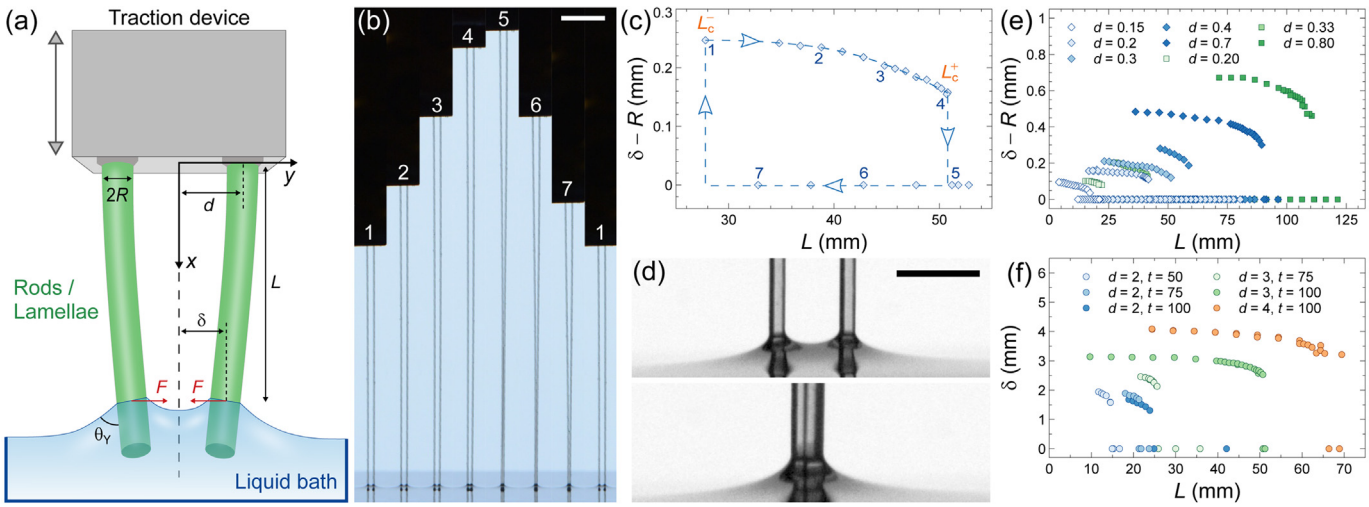

Fig. 1. (a) Schematic of the experimental set up. Two identical rods or lamellae are clamped vertically to a linear stage at a distance $2d$. They are partially immersed in a liquid bath with a dry length L and a contact angle θ_Y. Because of the capillary force F induced by the menisci, the distance between their free ends at the air–liquid interface is $2\delta < 2d$. The cylindrical rods are made of glass (PET) with a radius $R = 50 \pm 2$ μm (100 ± 2 μm), a Young modulus $E = 64 \pm 1$ GPa (10 ± 1 GPa), a density $\rho_s = 2500$ kg m^{-3} (1380 kg m^{-3}) and a total length $30 \leq L_0 \leq 200$ mm. The lamellae are made of PET with a thickness $23 \leq t \leq 250$ μm, width $10 \leq W \leq 30$ mm, total length $50 \leq L_0 \leq 300$ mm, Poisson ratio $\nu = 0.4$, $E = 5 \pm 0.5$ GPa and $\rho_s = 1380$ kg m^{-3}. (b) Snapshots of an experiment cycle for PET rods clamped at a distance $2d = 0.8$ mm. Scale bar: 5 mm. (c) Evolution of the distance $\delta - R$ as a function of the dry length L for the experiment shown in panel (b). (d) Fluid interface distortion induced by two PET rods when separated (top) or in contact (bottom). Scale bar: 1 mm. (e) Evolution of $(\delta - R)$ as a function of L for rods made of glass (diamond) and of PET (square) clamped at different distances d. (f) Evolution of δ as a function of L for PET lamellae of various thickness and clamped at different distances d. The distances d are given in mm and the thicknesses in μm.

distance $2d$, see Fig. 1(a). The lamellae are made of Polyethylene terephthalate (PET) and the rods are made of glass or PET. They are characterized by a Young modulus E, a density ρ_s and a total length L_0. The cylindrical rods have a radius R whereas the lamellae have a thickness t, a width W and a Poisson ratio ν (see Fig. 1 for the parameter values). Silicon oil with surface tension $\gamma = 0.021$ N m^{-1}, density $\rho_\ell = 960$ kg m^{-3} and viscosity $\mu = 10$ cSt is used as a model fluid. The viscosity was varied in few experiments ($10 < \mu < 1000$ cSt) without any noticeable impact on the results as expected. The fluid container is large compared to the spatial extension of the menisci to avoid border effects. For the lamellae, W was chosen large with respect to the capillary length to limit boundary effects. The width was varied to ensure that it did not affect the results.

Initially, the rods/lamellae are immersed in silicon oil deep enough such that they do not coalesce. They are quasi-statically withdrawn by steps of 1 mm at a speed of 20 mm/min. A picture is taken at each step by a computer controlled camera (Nikon D850) until coalescence is reached when $L = L_c^+$. The pair is then plunged back in the bath until they separate when $L = L_c^-$. Fig. 1(b) shows snapshots of a whole experiment cycle for rods. Note that to account for the potential slight deviation from parallelism between both structures, the distance $2d$ is also measured at the position L_c^+ when the pair is completely removed from the bath and yields small uncertainties on d.

2.2. Results

As the slender structures are immersed in a fluid of surface tension γ and density ρ_ℓ, the air–liquid interface is no longer flat and menisci form near them (Fig. 1(d)). They extend along the air–liquid interface over a distance proportional to the radius R for the rods or to the capillary length $\ell_c = (\gamma/\rho_\ell g)^{1/2}$ for the lamellae [44] (g is the gravitational acceleration). The two menisci being identical, their interaction yields an attractive shear force whose magnitude decreases when the distance between them increases [28–30]. Therefore, when the imposed distance between the elastic objects, d, is large compared to R for rods and to ℓ_c for lamellae, there is no significant interaction between them and the two structures stay parallel. When d is sufficiently small, the menisci interaction slightly bends the two structures so that their distance along the air–liquid interface, 2δ, is smaller than the imposed distance at the clamped ends, $2d$, see Fig. 1(a).

At the beginning of an experiment, the dry length L of the rods/lamellae is small so that their effective stiffness is large and they barely bend, i.e. $\delta \simeq d$. As L increases, the structures become progressively easier to bend and δ decreases. Fig. 1(c) shows the evolution of δ as a function of L obtained from a conventional image analysis of the experiment displayed in Fig. 1(b) for rods. The variation of δ is moderate when L is sufficiently small but becomes significant when L approaches a critical value, L_c^+, at which a contact between the structures occurs. The transition to coalescence appears to be discontinuous: at the transition length L_c^+, the gap $2(\delta - R)$ between the structures at the air–liquid interface jumps from a finite value to 0 as the dry length is incrementally increased. After coalescence, when the dry length is decreased, the free ends of the structures remain in contact until another critical length $L_c^- < L_c^+$ is reached, exhibiting a large hysteresis loop, and the gap jumps back to the previous branch (Fig. 1(c)).

Experiments have been performed with various type of slender structures and some representative variations of δ with L are shown in Fig. 1(e) for rods and (f) for lamellae. In all cases, there is a critical length L_c^+ beyond which coalescence is observed. Although this qualitative observation is valid for both rods and lamellae, there is a clear difference between both systems: rods tend to deflect relatively more than lamellae at the transition length L_c^+. The goal of the model developed in the next section is to accurately describe this bifurcation to coalescence for both types of structure, to determine the expression of L_c^+ as a function of the system control parameter and to construct a phase diagram delimiting the coalescence region.

Before developing the theoretical model, let us discuss the physical ingredients at play to determine the characteristic length scales. In this system, surface tension is the driving force of coalescence and elasticity the resisting force. The weight of the structures should nonetheless also be considered. Indeed, for very long structures, gravity appears as the dominating resisting force

to deflection. We thus expect the following characteristic lengths to play a role:

$$\ell_{BC} = [B/(\gamma P)]^{1/2}, \quad \ell_{BG} = [B/(\rho_s g S)]^{1/3}, \tag{1}$$

where P and S are respectively the perimeter and the area of the cross section of the structure and B is the bending stiffness ($B = \pi E R^4/4$ for rods and $B = Et^3 W/[12(1-\nu^2)]$ for lamellae). The bendocapillary and bendogravitational lengths, ℓ_{BC} and ℓ_{BG}, correspond, respectively, to the typical length above which capillary forces and gravity may bend a slender structure [3,45]. These characteristic lengths are directly measured using calibration experiments for lamellae (Appendix A).

3. Model

Since the deflections are small ($d/L \ll 1$), we use the linear beam equation to model the homogeneous rods or lamellae and consider the tension induced by surface tension and gravity. The capillary tension reads $T_\gamma = \gamma \cos\theta_Y P$, where θ_Y is the contact angle. We assume, for simplicity, that all the mass is concentrated at a distance L from the clamped end and neglect the weight of the immersed part of the structure so that the tension induced by gravity is given by $T_g = \rho_s g S L$. Using $\bar{x} = x/L$ and $\bar{w} = w/d$, the dimensionless linear beam equation for one of the two structures reads

$$\bar{w}''''(\bar{x}) - \alpha^2\, \bar{w}''(\bar{x}) = 0, \tag{2}$$

where $y = w(x)$ is the deflection of the structure, prime denotes a derivative with respect to $\bar{x}$ and $\alpha^2 = (T_\gamma + T_g)L^2/B = L^2 \cos\theta_Y/\ell_{BC}^2 + L^3/\ell_{BG}^3$ is the dimensionless tension. Since the top end of the structure is clamped and the bottom end is free with a transverse force acting on it, we have the following set of boundary conditions (BCs):

$$\bar{w}(0) = 1, \quad \bar{w}'(0) = 0, \quad \bar{w}''(1) = 0, \tag{3a}$$

$$\bar{w}'''(1) = \alpha^2 \bar{w}'(1) - \frac{FL^3}{Bd}, \tag{3b}$$

where F is the capillary force (Fig. 1(a)). The solution of Eqs. (2) and (3a) reads

$$\bar{w}(\bar{x}) = 1 - A\frac{\alpha\bar{x}\cosh\alpha - \sinh\alpha + \sinh(\alpha - \alpha\bar{x})}{\alpha\cosh\alpha - \sinh\alpha}, \tag{4}$$

where $A \geq 0$ is a dimensionless deflection coefficient at the air–liquid interface since

$$\delta/d = \bar{w}(1) = 1 - A, \quad \Rightarrow \quad Ad = d - \delta, \tag{5}$$

where $d - \delta$ is the displacement of the free end. Substituting Eq. (4) in the last BC (3b), we obtain

$$F_{el} \equiv k(d-\delta) = -F, \quad k = \frac{B}{L^3}\frac{\alpha^3}{\alpha - \tanh\alpha}, \tag{6}$$

which is just the balance between the capillary force F and an elastic force F_{el} with an effective spring constant k involving the bending modulus, the length and the tension of the structure.

The expression of the capillary forces F between two identical rigid rods ($R \ll \delta \ll \ell_c$) or lamellae ($\delta \ll \ell_c$) has been derived and compared to experiments in the literature [28,31,34]. They read as:

$$F_R(\delta) = -\pi\gamma R^2 \cos^2\theta_Y \left[\delta^2 - R^2\right]^{-1/2}, \tag{7a}$$

$$F_L(\delta) = -(\gamma/2) W \cos^2\theta_Y\, (\delta/\ell_c)^{-2}, \tag{7b}$$

where the subscripts R and L refer respectively to rods and lamellae. The capillary force scales as δ^{-1} for rods and δ^{-2} for lamellae and have distinct characteristic lengths, i.e. R for rods and ℓ_c for lamellae. Eqs. (7) are no longer valid when $\delta \gtrsim \ell_c$ since the forces decrease exponentially at large distance [30,32]. Nevertheless, Eqs. (7) are sufficient for our study because such large distances between the two structures are not considered in the experiments. Indeed, since the capillary forces are exponentially small at large distance, coalescence is possible only if the effective stiffness of the structures is small enough. However, Eq. (6) together with the definition of α show that k cannot be smaller than $B/L_{BG}^3 = \rho_s g S$ during a given experiment where only the dry length L is varied. Therefore, when $\delta \gtrsim \ell_c$, the capillary forces are not strong enough to significantly bend the structures we use and promote aggregation. Note that, in principle, the shape of the menisci, and hence the resulting force, change when the structures deform and get slightly tilted at the interface. This effect is neglected here. Note also that a 2D description for the lamellae is possible if $W \gtrsim \ell_c$ so that the influence of the menisci generated by the edges is negligible compared to the force (7b) induced by the menisci created by the faces.

Substituting the expressions (7) of the forces in the equilibrium equation (6) and using Eq. (5) to eliminate δ, we obtain an equation for A for both rods and lamellae:

$$A\bar{d}_R\sqrt{\bar{d}_R^2(1-A)^2 - 1} \equiv H_R(A, \bar{d}_R) = \Lambda_R \equiv \Lambda/R, \tag{8a}$$

$$2A\bar{d}_L^3(1-A)^2 \equiv H_L(A, \bar{d}_L) = \Lambda_L \equiv \Lambda/\ell_c, \tag{8b}$$

$$\Lambda = \left[\frac{L^3\cos^2\theta_Y}{2\ell_{BC}^2}\right]\left[\frac{\alpha - \tanh\alpha}{\alpha^3}\right], \tag{8c}$$

$$\bar{d}_R = \frac{d}{R}, \quad \bar{d}_L = \frac{d}{\ell_c}, \quad \alpha^2 = \frac{L^2}{\ell_{BC}^2}\cos\theta_Y + \frac{L^3}{\ell_{BG}^3}, \tag{8d}$$

where Λ is a rescaled dry length. The functions H_R and H_L are shown in Fig. 2 as a function of A for given values of $\bar{d}_R$ and $\bar{d}_L$ together with the total rescaled energy of the system for rods ($\bar{U}_R$) and lamellae ($\bar{U}_L$) (Appendices B, C)

$$\bar{U}_R = \frac{A^2}{2} + \frac{\Lambda_R}{\bar{d}_R^2}\ln\left[\bar{d}_R(1-A) + \sqrt{\bar{d}_R^2(1-A)^2 - 1}\right], \tag{9a}$$

$$\bar{U}_L = \frac{A^2}{2} - \frac{\Lambda_L}{2\bar{d}_L^3(1-A)}. \tag{9b}$$

The function H_R vanishes at $A = 0$ and $A = 1 - \bar{d}_R^{-1}$ and has a maximum value, Λ_R^c, at an intermediate value A_R^c, see Fig. 2(a)–(c). When $\Lambda_R < \Lambda_R^c$, Eq. (8a) admits two solutions for A (Fig. 2(a)). The largest one corresponds to a local maximum of the energy and is unstable. The energy is also characterized by two local minima. We thus expect bistability between an open state given by the smallest solution of Eq. (8a) and a contact state with $A = 1 - \bar{d}_R^{-1}$, i.e. $\delta = R$. When Λ_R approaches Λ_R^c, by increasing the dry length L, both solutions of Eq. (8a) get closer until they merge when $\Lambda_R = \Lambda_R^c$ (Fig. 2(b)). When Λ_R is infinitesimally larger than Λ_R^c, Eq. (8a) does not have any solution and the energy is characterized by only one local minimum at $A = 1 - \bar{d}_R^{-1}$ (Fig. 2(c)). The deflection A then jumps from A_R^c, corresponding to an open state, to contact. There is thus a discontinuous, subcritical transition to coalescence. The function H_L is similar to H_R since it vanishes at $A = 0$ and at $A = 1$ and has a maximum value Λ_L^c at an intermediate value A_L^c, see Fig. 2(d)–(f). Therefore, a similar reasoning applies to lamellae.

The position and value of the maximum of the functions H_R (in the limit $\bar{d}_R \gg 1$) and H_L given by Eqs. (8a) and (8b) are

$$A_R^c = \frac{1}{2}, \quad \Lambda_R^c = \frac{\bar{d}_R^2}{4} - \frac{1}{2}, \quad A_L^c = \frac{1}{3}, \quad \Lambda_L^c = \frac{8\bar{d}_L^3}{27}, \tag{10}$$

where terms of order $\bar{d}_R^{-2}$ have been omitted for rods. The expressions for A_i^c show that rods deflect to half their initial distance before snapping into contact whereas lamellae deflect to only one

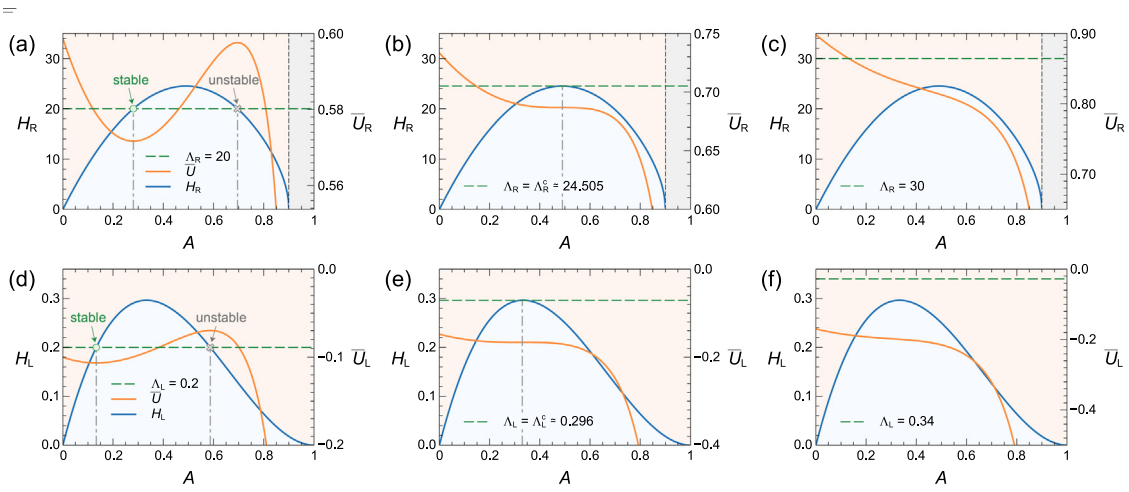

Fig. 2. (a)–(c) Evolution of $H_R(A, \bar{d}_R)$, defined by Eq. (8a) (blue curve), and of the total energy $\bar{U}_R(A, \bar{d}_R, \Lambda_R)$, defined by Eq. (9a) (orange curve), as a function of the deflection parameter A for $\bar{d}_R = 10$. When $\Lambda_R < \Lambda_R^c \simeq 24.5$, Eq. (8a) admits two solutions corresponding to local extrema of $\bar{U}$. The smallest is stable and describes an open state. When $\Lambda_R > \Lambda_R^c$, there is no solution to Eq. (8a) and $A = 1 - \bar{d}_R^{-1}$ (contact state). (d)–(f) Corresponding situation for lamellae for $\bar{d}_L = 1$ with $H_L(A, \bar{d}_L)$ and $\bar{U}_L(A, \bar{d}_L, \Lambda_L)$ given respectively by Eqs. (8b) and (9b). (For interpretation of the references to color in this figure legend, the reader is referred to the web version of this article.)

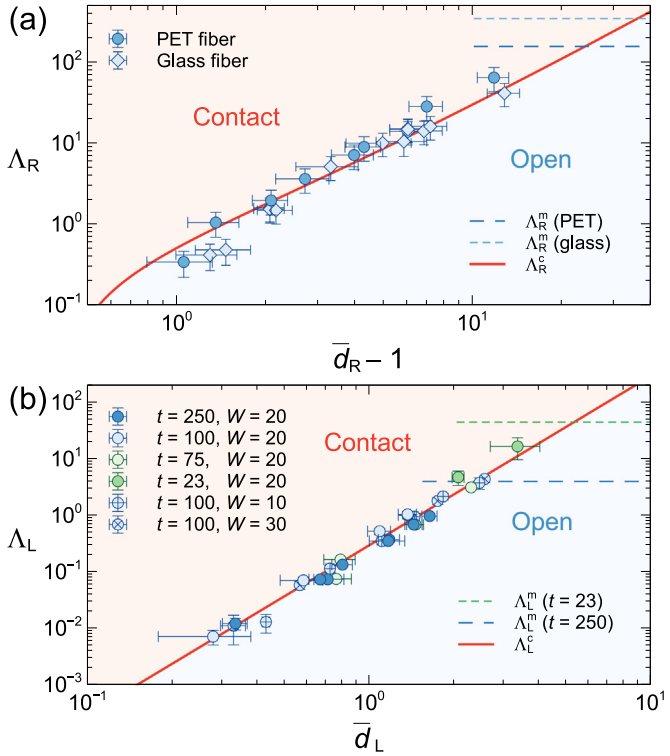

Fig. 3. Coalescence phase diagrams for rods (a) and lamellae (b) where $\bar{d}_R = d/R \geq 1$ and $\bar{d}_L = d/\ell_c \geq 0$ respectively. The symbols represent experimental data corresponding to the largest dry length reached in each experiment before coalescence occurs. The curves Λ_R^c and Λ_L^c given by Eqs. (10) are shown together with the maximum value of Λ_R and Λ_L given by Eqs. (16). The thicknesses t are given in μm and the widths W in mm.

third of this distance. The curve $\Lambda_i^c(\bar{d}_i)$ thus delimits the region where coalescence occurs in the phase diagram spanned by the parameters $\bar{d}_i$ and Λ_i with $i = R$ or L. Fig. 3 shows a good agreement between the theoretical expressions (10) and the data except when the distance between rods becomes comparable to their radius. In this regime, Eq. (7a) underestimates the capillary force between rods [34] and coalescence occurs with a dry length smaller than predicted here.

To draw the bifurcation diagrams, we use Λ_R and Λ_L as bifurcation parameters and

$$\eta_R = \frac{\delta - R}{d - R} = 1 - \frac{A}{1 - \bar{d}_R^{-1}}, \quad \eta_L = \frac{\delta}{d} = 1 - A, \tag{11}$$

as order parameters. The diagrams may be obtained by solving Eqs. (8a) and (8b) to get A, and thus the order parameters, as a function of Λ_R and Λ_L respectively for a given distance d between the structures. It is however possible to obtain simple analytical expressions near the bifurcation point by expanding the functions H_R and H_L around their maximum

$$H_i \simeq \Lambda_i^c + \frac{1}{2}\frac{\partial^2 H_i}{\partial A^2}\Big|_{A=A_i^c}(A - A_i^c)^2, \quad i = R, L. \tag{12}$$

Eqs. (8a) and (8b) can then be solved to obtain A and the order parameters (11) as a function of Λ_i:

$$2\eta_R \simeq 1 \pm \sqrt{1 - \frac{4\Lambda_R}{\bar{d}_R^2}}, \quad \frac{3\eta_L}{2} \simeq 1 \pm \sqrt{\frac{1}{3} - \frac{9\Lambda_L}{8\bar{d}_L^3}}, \tag{13}$$

Fig. 4 shows that these simple asymptotic expressions enable us to obtain a collapse of the bifurcation data when the order parameters η_R and η_L are plotted as a function of the new bifurcation parameters $\Lambda_R/\bar{d}_R^2$ and $\Lambda_L/\bar{d}_L^3$ respectively.

4. Discussion and conclusion

The characteristic length Λ given by Eq. (8c) appears as the parameter containing the physics at play in the coalescence process. During a given experiment, all the parameters are fixed except L which increases. Since Λ increases monotonically with L, there is an unambiguous relationship between both quantities. This length scale is composed of two factors written between square brackets in Eq. (8c). The first one does not contain the tension coefficient α and scales as L^3. It compares the beam stiffness ($\sim B/L^3$) to the surface tension γ. The second one depends on the dimensionless tension α which is a function of L. The relation

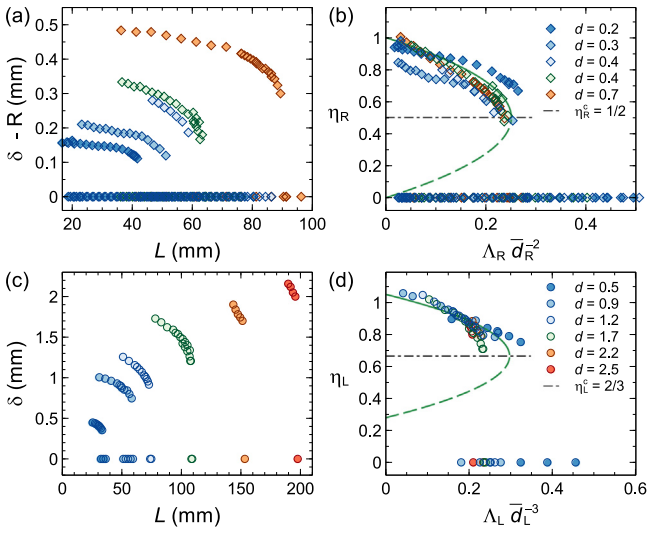

Fig. 4. Experimental bifurcation data for glass rods (a) and PET lamellae with $t = 250$ μm (c). (b)–(d) Rescaling of the data according to the asymptotic master curves given by Eqs. (13). The initial gap d is given in mm.

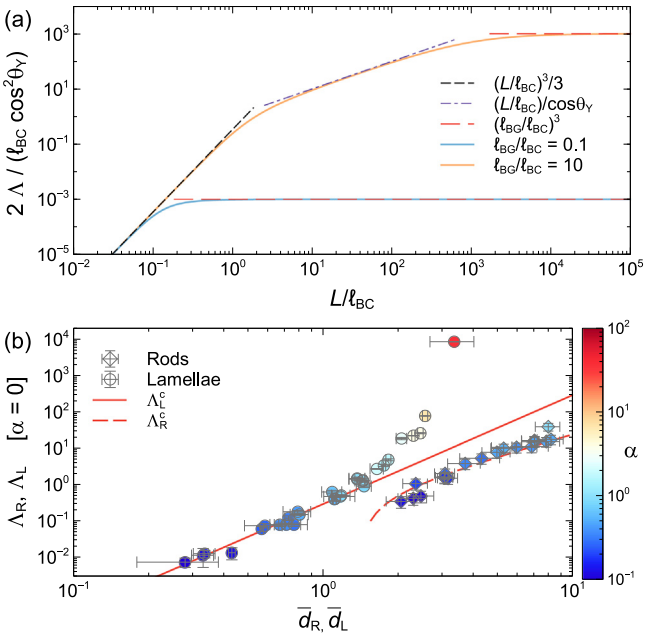

Fig. 5. (a) Evolution of $\bar{\Lambda} = 2\Lambda/(\ell_{BC}\cos^2\theta_Y)$ as a function of L/ℓ_{BC} for $\theta_Y = 0$. When $\ell_{BG}/\ell_{BC} \ll 1$, $\bar{\Lambda}$ grows like $(L/\ell_{BC})^3$ before to saturate at $\bar{\Lambda}^m = (\ell_{BG}/\ell_{BC})^3$ when $L \gtrsim \ell_{BC}$. When $\ell_{BG}/\ell_{BC} \gg 1/\sqrt{\cos\theta_Y}$, there is an intermediate regime where $\bar{\Lambda} \simeq (L/\ell_{BC})/\cos\theta_Y$ when $\ell_{BC}/\sqrt{\cos\theta_Y} \ll L \ll \cos\theta_Y\,\ell_{BG}^3/\ell_{BC}^2$. (b) Coalescence phase diagrams for rods and lamellae where Λ_R and Λ_L, defined by Eqs. (8), are computed with $\alpha = 0$, i.e. when tension is neglected. The colorbar indicates the value of α for each data point. A good agreement between experiments and theory (Eqs. (10)) is achieved only when $\alpha \lesssim 1$ as expected. In this case, the expression of L_c^+ is given by Eqs. (15). (For interpretation of the references to color in this figure legend, the reader is referred to the web version of this article.)

between Λ and L is thus intricate as illustrated in Fig. 5(a). Nevertheless, this relation simplifies in some asymptotic limits according to the value of α:

$$\Lambda \underset{\alpha\ll 1}{=} \frac{L^3\cos^2\theta_Y}{6\ell_{BC}^2}, \quad \Lambda \underset{\alpha\gg 1}{=} \frac{L^3\cos^2\theta_Y}{2\alpha^2\,\ell_{BC}^2}. \tag{14}$$

The first limit $\alpha \ll 1$ corresponds to $L \ll \min(\ell_{BG}, \ell_{BC})$. In this regime where tension is negligible, the expression of L_c^+ may be explicitly derived from $\Lambda_i = \Lambda_i^c$ with Λ_i^c given in Eqs. (10)

$$[L_c^+]^3 = \frac{3B}{2\pi\gamma\cos^2\theta_Y}\left[\frac{d^2}{2R^2} - 1\right], \quad [L_c^+]^3 = \frac{8(B/W)d^3}{9\gamma\cos^2\theta_Y\ell_c^2}, \tag{15}$$

where the first equality stands for rods and the second for lamellae. For given slender structures, these expressions show that L_c^+ is small enough to have $\alpha \ll 1$ when d is small enough. Fig. 5(b) shows indeed a good agreement between theory and experiments when the structures are close enough. In our experiments, significant deviation from the theory without tension occurs only for lamellae.

The second limit $\alpha \gg 1$ corresponds to $L \gg \max(\ell_{BG}, \ell_{BC})$ so that $\alpha^2 \simeq (L/\ell_{BG})^3$. Therefore, Eq. (14) shows that Λ saturates to a constant value Λ^m for long structures

$$\Lambda^m = \frac{\ell_{BG}^3\cos^2\theta_Y}{2\ell_{BC}^2} = \frac{\gamma\cos^2\theta_Y}{\rho_s g}\frac{P}{2S}, \tag{16}$$

where we used Eq. (1) and $P/(2S)$ is equal to R^{-1} for rods and t^{-1} for lamellae. Eq. (16) results from the interplay between the horizontal capillary shear force promoting coalescence and the vertical gravitational force hindering aggregation. A necessary condition to observe coalescence is thus $\Lambda_i^m > \Lambda_i^c$. Using Eqs. (10) and (16), we obtain

$$d^2 < \frac{4\gamma\cos^2\theta_Y}{\rho_s g}, \quad d^3 < \frac{27\gamma\cos^2\theta_Y\ell_c^2}{8\rho_s g\,t}, \tag{17}$$

for rods and lamellae respectively. These expressions give the maximum imposed distance d beyond which coalescence is not possible. The upper limits $\Lambda_R^m = \Lambda^m/R$ and $\Lambda_L^m = \Lambda^m/\ell_c$ are shown as horizontal dashed lines in Fig. 3. These limits have almost been reached in the experiments. This justifies the use of Eqs. (7) neglecting the exponential tail of the capillary force. Indeed, this tail can only be probed by increasing the imposed distance d between the structures which is already close to the limits (17) in our experiments.

Finally, if $\ell_{BG}/\ell_{BC} \gg 1/\sqrt{\cos\theta_Y}$, Eq. (8d) shows that α can be much larger than 1 with $\alpha^2 \simeq (L/\ell_{BC})^2\cos\theta_Y$ when $1/\sqrt{\cos\theta_Y} \ll L/\ell_{BC} \ll (\ell_{BG}/\ell_{BC})^3\cos\theta_Y$. Therefore, in this case, there is an intermediate regime before the saturation of Λ where $2\Lambda = L\cos\theta_Y$, see Fig. 5(a). In our experiments, $\ell_{BG} < \ell_{BC}$ and such a regime is not observed (see Table A.1).

The fully analytical model developed here is based on the linear beam theory, as the maximum deflection d is very small compared to the dry length L in the experiments. In Appendix D, we derive a model based on the nonlinear beam theory to determine the domain of validity of the linear model presented above. We show that the linear theory is always essentially valid. Small differences between the linear and nonlinear theories occur only in the case of very soft and small structures.

The length L_c^- at which the two structures separate when re-immersed in the liquid bath cannot be derived within this framework. Indeed, for both rods and lamellae, the contact state is stable for all values of the dry length in this theory since it always corresponds to a local minimum of the total energy. This problem comes from the transverse capillary force computed from the interaction between vertical structures. A contact state is thus associated to a contact zone extending over all the structure length which overestimates the capillary force. The dry length $L_c^- < L_c^+$, for which two structures in contact detach is actually known and corresponds to the dry length of the equilibrium

shape of capillary aggregated pair of lamellae [3,46] and fibers [5]. This length depends on the total length of the structures, which enables or not tangential contact at the free end, as studied in Ref. [46].

This work is a first step toward understanding the elasto-capillary coalescence of slender structures in fluid capture by brush-like systems. A complete understanding requires to study the influence of an array of fibers and/or the retraction speed on the coalescence as the structures are withdrawn from a bath. Preliminary results indicate that the retraction speed significantly impacts the coalescence process. On one hand, the surface energy, and hence the capillary force, is increased by the formation of a Landau–Levich film around the structures. On the other hand, if the structures are removed too swiftly from the bath, they have not enough time to get into contact. Rationalizing these antagonistic effects would contribute to better understand the coalescence process in such a system and its impact on the amount of fluid captured.

Declaration of competing interest

The authors declare that they have no known competing financial interests or personal relationships that could have appeared to influence the work reported in this paper.

Data availability

Data will be made available on request.

Acknowledgments

The authors acknowledge support by F.R.S.-FNRS under the research grant (PDR "ElastoCap") n° T.0025.19. This project has received funding from the European Union's Horizon 2020 research and innovation programme under the Marie Sklodowska-Curie grant agreement n° 101027862.

Appendix A. Characteristic length scales

Determining ℓ_{BC}

As reported in Ref. [47], estimating the bendocapillary length ℓ_{BC} for lamellae using each parameter involved in Eq. (1) of the main text produces large errors. Therefore, we directly measure this length scale with the following calibration experiment.

We clamp two identical parallel lamellae at a distance $2d$, deposit a droplet of silicon oil on one of the lamellae and bring them into contact. As the PET sheets used for this study are relatively stiff, folding them to form a loop with a self-contacting tail, as proposed in Ref. [47], would require meter-long lamellae and is therefore hardly applicable. The clamping distance is varied for a given pair of lamellae and the length L at which lamellae join in tangential contact is measured, see Fig. A.6(a)–(b).

To determine ℓ_{BC}, we compute theoretically the evolution of L as a function of d. As L is large compared to the clamping distance ($d/L \ll 1$) and smaller than ℓ_{BG}, we use a linear beam equation and neglect gravity to describe the shape of the lamellae. The equation to solve reduces to $w^{(4)}(x) = 0$, where $y = w(x)$ is the deflection of one of the two lamellae, with the BCs: $w(0) = d$, $w'(0) = w(L) = w'(L) = 0$, see Fig. A.6(a). The solution reads as $w(x) = d(L-x)^2(L+2x)/L^3$. The length L is fixed thanks to an additional BC obtained as follow.

Considering a small virtual displacement dx of the tangential contact point at $x = L$, the variation of bending energy may be written as $dE_B = B\kappa_c^2 dx$, where κ_c is the curvature at the contact point [47]. The variation of interfacial energy reads $dE_S = 2\gamma \cos\theta_Y W dx$, where θ_Y is the contact angle of the liquid on the surface (equal to zero in our case). Equating both energy variations yields the curvature at the contact point $\kappa_c = \sqrt{\cos\theta_Y}/\ell_{BC}$ ($P \simeq 2W$). Imposing $w''(L) = \kappa_c$, with $w(x)$ derived above, we obtain L as a function of d and the bendocapillary length ℓ_{BC}:

$$L = \left(\frac{6\ell_{BC} d}{\sqrt{\cos\theta_Y}}\right)^{1/2}. \tag{A.1}$$

The length ℓ_{BC} is then adjusted so that Eq. (A.1) fits the measured dry lengths for each thickness considered, see Fig. A.6(b). Fig. A.6(a) shows that the resulting theoretical shape agrees well with the lamella shape.

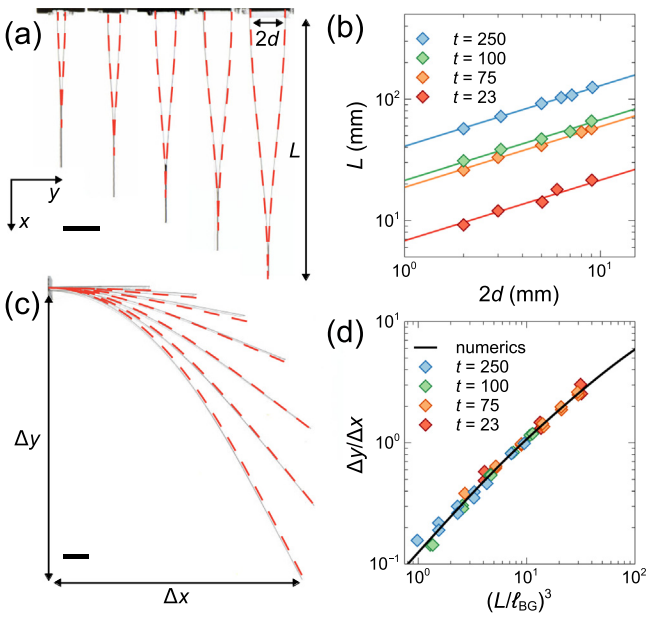

Fig. A.6. Experimental determination of the characteristic lengths ℓ_{BC} and ℓ_{BG}. (a) Sticking length L of two PET lamellae ($t = 100$ μm) for various gaps d. Dashed lines correspond to the linear beam theory. Scale bar: 10 mm. (b) L as a function of d for lamellae of various thickness t (μm). Fitting the experimental points with Eq. (A.1) (solid curves) yields the bendocapillary length ℓ_{BC} for each thickness. (c) Lamellae of various length L deflected by their own weight. Dashed lines correspond to the numerical solution of Eq. (A.2a). Scale bar: 10 mm. (d) Deflection ratio $\Delta y/\Delta x$ as a function of $(L/\ell_{BG})^3$ for lamellae of various thicknesses. Adjusting the experimental data to the numerical master curve obtained from Eqs. (A.2), yields the bendogravitational length ℓ_{BG}.

Determining ℓ_{BG}

We perform the following experiments to measure ℓ_{BG} [48]. Lamellae of various lengths L are clamped horizontally at one end and are deflected by their own weight, see Fig. A.6(c). As the deflections are a priori large, we turn to the nonlinear elastica description of the lamella deformation. Using the arclength s and θ, the local angle between the tangent to the lamella and the horizontal axis, to parametrize the lamella, we have:

$$\frac{d^2\theta}{d\bar{s}^2} = \frac{L^3}{\ell_{BG}^3}(\bar{s}-1)\cos\theta, \quad \theta(0) = \theta'(1) = 0, \tag{A.2a}$$

$$\Delta x = \int_0^1 \cos\theta(\bar{s})\, d\bar{s}, \quad \Delta y = \int_0^1 \sin\theta(\bar{s})\, d\bar{s}, \tag{A.2b}$$

where $\bar{s} = s/L$. This equation is integrated using a shooting method and the resulting deflection of the free end, Δx and Δy, is computed as a function of L/ℓ_{BG}. The bendogravitational length

of our lamellae is obtained by adjusting the data to the numerical master curve, see Fig. A.6(d).

In the case of rods, such calibration tests are not performed, as their mechanical and geometrical properties are well characterized and guaranteed by the suppliers (Hildenberg for the glass rods, Goodfellow for the PET rods).

Table A.1 gives the values of ℓ_{BC} and ℓ_{BG} for structures considered in this work.

Table A.1
Bendocapillary and bendogravitational lengths of lamellae and rods used in this work. The values for rods have been computed using Eq. (1) of the main text and error propagation. The thickness and radius are given in μm and ℓ_{BC} and ℓ_{BG} are given in mm.

Lamellae			Rods		
t	ℓ_{BC}	ℓ_{BG}	R	ℓ_{BC}	ℓ_{BG}
23	16 ± 2	25 ± 2	50	218 ± 6	118 ± 2
75	118 ± 4	58 ± 3	100	244 ± 14	123 ± 4
100	153 ± 10	73 ± 3			
250	557 ± 12	120 ± 10			

Appendix B. Capillary force and total energy: rods

Capillary force

The authors in Ref. [28] computed the difference of surface energy between a configuration where two vertical and cylindrical rods of radius R are at an infinite distance and a configuration where the two symmetry axes of the rods are at a finite distance 2δ. The following expression is valid provided R and δ are small enough compared to the capillary length ($\ell_c = (\gamma/\rho_\ell g)^{1/2}$) and θ_Y close enough to $\pi/2$:

$$U_S = -2\pi\gamma R\cos\theta_Y\,(h_c - h_\infty), \tag{B.1a}$$

$$h_\infty = R\cos\theta_Y\,\ln\left[\frac{4}{\gamma_e(1+\sin\theta_Y)R/\ell_c}\right], \tag{B.1b}$$

$$h_c = R\cos\theta_Y\left[\tau_1 + 2\ln\left[\frac{1-\exp(-2\tau_1)}{\gamma_e a/\ell_c}\right]\right], \tag{B.1c}$$

$$\tau_1 = \ln\left[\frac{a}{R} + \sqrt{1+\frac{a^2}{R^2}}\right], \quad a = \sqrt{\delta^2 - R^2}, \tag{B.1d}$$

where $\gamma_e \simeq 1.781$ ($\ln\gamma_e$ is the Euler–Mascheroni constant).

This expression can be written in a simpler form by writing $\bar{h}_c = h_c/(R\cos\theta_Y)$ as

$$\bar{h}_c = \tau_1 + 2\ln\left[\frac{1-\exp(-2\tau_1)}{a/R}\right] - 2\ln(\gamma_e R/\ell_c). \tag{B.2}$$

Using the definition (B.1d) of τ_1 and a, we get

$$\bar{h}_c = -\ln\left(\frac{\delta}{R} + \sqrt{\frac{\delta^2}{R^2}-1}\right) - 2\ln\left(\frac{\gamma_e R}{2\ell_c}\right). \tag{B.3}$$

Therefore, the surface energy can be written as

$$\frac{U_S}{2\pi\gamma R^2\cos^2\theta_Y} = \ln\left[\frac{\delta}{R} + \sqrt{\frac{\delta^2}{R^2}-1}\right] + C, \tag{B.4a}$$

$$C = \ln\left(\frac{\gamma_e R}{(1+\sin\theta_Y)\ell_c}\right). \tag{B.4b}$$

The capillary force is given by $2F = -\partial(U_S)/\partial\delta$:

$$F(\delta) = -\pi\gamma R^2\cos^2\theta_Y\left[\delta^2 - R^2\right]^{-1/2}. \tag{B.5}$$

This expression coincides with Eq. (7a) of the main text.

Total energy

The total energy, U_R, of half the system is given by

$$\begin{aligned} U_R &= U_B + U_T + \frac{U_S}{2}, \\ &= \frac{B}{2}\int_0^L [w''(x)]^2\,dx + \frac{T}{2}\int_0^L [w'(x)]^2\,dx + \frac{U_S}{2}. \end{aligned} \tag{B.6}$$

Using the expression of w given by Eq. (4) of the main text, and the expression (B.4) of U_S (with $\delta = d(1-A)$), we get

$$\begin{aligned} U_R(A) = {} & \frac{BA^2d^2}{4L^3}\frac{\alpha^3(-\alpha+\cosh\alpha\sinh\alpha)}{(-\alpha\cosh\alpha+\sinh\alpha)^2} \\ & + \frac{TA^2d^2}{8L}\frac{\alpha\,[2\alpha(2+\cosh 2\alpha) - 3\sinh 2\alpha]}{(-\alpha\cosh\alpha+\sinh\alpha)^2} \\ & + \pi\gamma R^2\cos^2\theta_Y\,(\ln g(A) + C), \end{aligned} \tag{B.7}$$

$$g(A) = \bar{d}_R(1-A) + \sqrt{\bar{d}_R^2(1-A)^2 - 1}, \quad \bar{d}_R = \frac{d}{R}.$$

The tension T can be eliminated in favor of α by using its definition, namely $\alpha^2 = TL^2/B$ (see below Eq. (2) of the main text). The expression of the energy reduces to

$$U_R(A) = \frac{BA^2d^2}{2L^3}\frac{\alpha^3}{\alpha-\tanh\alpha} + \pi\gamma R^2\cos^2\theta_Y\,(\ln g(A) + C). \tag{B.8}$$

Defining the rescaled energy as

$$\bar{U}_R = \frac{U_R - \pi\gamma R^2\cos^2\theta_Y\,C}{\beta}, \quad \beta = \frac{Bd^2}{L^3}\frac{\alpha^3}{\alpha-\tanh\alpha}, \tag{B.9}$$

we have

$$\bar{U}_R(A) = \frac{A^2}{2} + \frac{\Lambda_R}{\bar{d}_R^2}\ln\left[\bar{d}_R(1-A) + \sqrt{\bar{d}_R^2(1-A)^2 - 1}\right], \tag{B.10}$$

where Λ_R is defined by Eq. (8) of the main text. We thus recover Eq. (9a) of the main text. The selected value of A is the one that minimizes the energy which is obtained from the equation

$$\frac{\partial\bar{U}_R}{\partial A} = 0 = A - \frac{\Lambda_R}{\bar{d}_R\sqrt{\bar{d}_R^2(1-A)^2 - 1}}. \tag{B.11}$$

We recover Eq. (8a) of the main text.

Appendix C. Capillary force and total energy: lamellae

Action and Lagrangian of the system

The surface energy in the region $0 \le x < \delta$ of the system depicted in Fig. C.7 reads

$$U_S = \gamma\,\ell\,W, \tag{C.1}$$

where ℓ is the length of the air–liquid interface in this region. The gravitational energy reads

$$U_G = \frac{\rho_\ell\,g\,W}{2}\int_0^\delta h(x)^2\,dx. \tag{C.2}$$

Therefore the dimensionless action is given by

$$\bar{\mathcal{S}} = \bar{\ell} + \frac{1}{2}\int_0^{\bar{\delta}} \bar{h}(\bar{x})^2\,d\bar{x}, \tag{C.3}$$

where $\bar{\mathcal{S}} = \mathcal{S}/(\gamma\,\ell_c W)$ and all lengths have been rescaled by the capillary length ℓ_c.

The action can now be written as the integral of a Lagrangian:

$$\bar{\mathcal{S}} = \int_0^{\bar{\delta}} \mathcal{L}(\bar{h},\bar{h}')\,d\bar{x}, \quad \mathcal{L} = \left[1+\bar{h}'^2\right]^{1/2} + \frac{\bar{h}^2}{2}, \tag{C.4}$$

where $\bar{h}' = d\bar{h}/dx$.

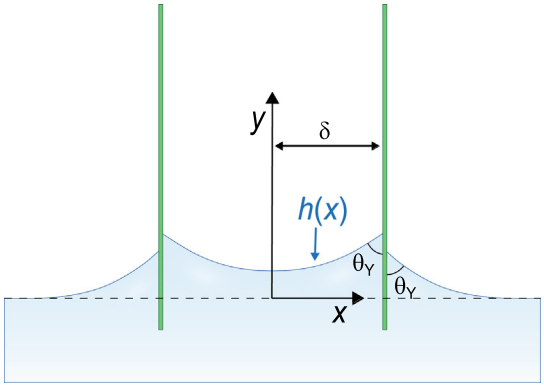

Fig. C.7. Schematic of the system composed of two lamellae separated by a distance 2δ.

Equation for the interface

The equation for the interface is obtained from the Euler–Lagrange equation:

$$\frac{\partial \mathcal{L}}{\partial h} - \frac{d}{d\bar{x}}\left(\frac{\partial \mathcal{L}}{\partial h'}\right) = 0. \tag{C.5}$$

We have

$$\bar{h} = \frac{\bar{h}''}{\left[1+\bar{h}'^2\right]^{\frac{3}{2}}}, \quad \bar{h}'(0) = 0,\ \bar{h}'(\bar{\delta}) = \cot\theta_Y, \tag{C.6}$$

which is the standard equation giving the shape of a meniscus and expresses the balance between the hydrostatic and Laplace pressures [44, p. 44–45].

Surface energy

By definition, the Hamiltonian reads

$$\mathcal{H} = \bar{h}'\frac{\partial \mathcal{L}}{\partial \bar{h}'} - \mathcal{L}. \tag{C.7}$$

Using Eq. (C.4), we get

$$\mathcal{H} = -\left[1+\bar{h}'^2\right]^{-1/2} - \frac{\bar{h}^2}{2}. \tag{C.8}$$

Since the Lagrangian does not depend explicitly on $\bar{x}$, the Hamiltonian is a constant. Therefore, the energy reads

$$\bar{U}_S = \int_0^{\bar{\delta}} \mathcal{H}\, d\bar{x} = \bar{\delta}\,\mathcal{H}(\bar{y}), \quad 0 \le y \le \bar{\delta}. \tag{C.9}$$

If we choose $\bar{y} = 0$ and use the first BC in Eq. (C.6), we get

$$\bar{U}_S = -\bar{\delta}\left(1 + \frac{\bar{h}^2(0)}{2}\right). \tag{C.10}$$

The energy, $\bar{U}_0$, when both lamellae are infinitely separated is obtained by setting $\bar{h}(0) = 0$, so that $\bar{U}_0 = -\bar{\delta}$. So finally, the relevant energy, $\bar{U}_S - \bar{U}_0$, is given by

$$\bar{U}_S = -\frac{\bar{\delta}\,\bar{h}^2(0)}{2} \quad \Rightarrow \quad \bar{F} = -\frac{\partial \bar{U}_S}{\partial \bar{\delta}}, \tag{C.11}$$

where we keep the same notation for the energy for simplicity. Note that there is no factor 1/2 in the expression of the force because the energy is computed for half of the system (in contrast to rods).

Shape of the air–liquid interface

Eq. (C.11) requires $\bar{h}(0)$ to be known to compute the capillary force. Therefore, we need to compute $\bar{h}(\bar{x})$ by solving Eq. (C.6). We start by computing the meniscus profile when the interface is almost planar (linear problem with $\theta_Y \simeq \pi/2$ and δ arbitrary). We then address the nonlinear problem. However, the expression of the energy, and hence the force, cannot be obtained explicitly. Therefore, we derive the asymptotic expression of the energy valid when $\delta \ll \ell_c$ and θ_Y arbitrary and propose an approximate expression of the energy matching both the linear solution and the asymptotic one. The comparison between the energy obtained by solving numerically the nonlinear problem and the approximate expression shows a good agreement.

Linear problem. Here, we assume that the contact angle is close to $\pi/2$ so that the interface is almost planar and $\bar{h}' \ll 1$. Eq. (C.6) becomes

$$\bar{h} = \bar{h}'', \quad \bar{h}'(0) = 0,\ \bar{h}'(\bar{\delta}) = \cot\theta_Y. \tag{C.12}$$

The solution reads

$$\bar{h}(\bar{x}) = \frac{\cot\theta_Y}{\sinh\bar{\delta}}\cosh(\bar{x}). \tag{C.13}$$

The energy is obtained from Eq. (C.11) and reads

$$\bar{U}_S = -\frac{\bar{\delta}\cot^2\theta_Y}{2\sinh^2\bar{\delta}}. \tag{C.14}$$

Nonlinear problem: equations. By definition, $\bar{h}' = \tan\theta$ where $\theta(\bar{s})$ is the local angle between the tangent to the interface and the horizontal x-axis and $\bar{s}$ is the arc length varying between 0 and $\bar{\ell}$. We also have $d\bar{x}/d\bar{s} = \cos\theta$ and $d\bar{h}/d\bar{s} = \sin\theta$. Therefore, Eq. (C.6) becomes

$$\bar{h} = \frac{d\theta}{d\bar{s}}, \quad \theta(0) = 0,\ \theta(\bar{\ell}) = \pi/2 - \theta_Y, \tag{C.15}$$

Deriving both sides with respect to $\bar{s}$, we finally have

$$\frac{d^2\theta}{d\bar{s}^2} = \sin\theta(\bar{s}), \quad \theta(0) = 0,\ \theta(\bar{\ell}) = \pi/2 - \theta_Y, \tag{C.16a}$$

$$\bar{x}(\bar{s}) = \int_0^{\bar{s}} \cos\theta(\bar{s}')\,d\bar{s}', \quad \bar{h}(\bar{s}) = \int_0^{\bar{s}} \sin\theta(\bar{s}')\,d\bar{s}' + \theta'(0), \tag{C.16b}$$

$$\bar{U}_S = -\frac{\bar{\delta}\,[\theta'(0)]^2}{2}, \tag{C.16c}$$

where we used Eq. (C.15) in the two last equations. The equation for θ is, up to a sign, the equation of a simple pendulum.

Nonlinear problem: solution. Eq. (C.16a) can be solved exactly

$$\theta(\bar{s}) = 2\arccos\left[q\,\mathrm{sn}(\bar{s}+\bar{s}_0, q)\right], \tag{C.17}$$

The function sn is a Jacobi elliptic function with a period $4K(q)$ where K is an elliptic function of the first kind [49, p. 549]. The quantities q and $\bar{s}_0$ are two constants of integration which are fixed by the BCs. The standard interval of possible values of q is $0 \le q < 1$. However, using the BC $\theta(0) = 0$, Eq. (C.17) yields $q\,\mathrm{sn}(\bar{s}_0, q) = 1$. Because $-1 \le \mathrm{sn} \le 1$, this last equation requires $q \ge 1$. Therefore, we use the following property [49, p. 563]

$$q\,\mathrm{sn}(x, q) = \mathrm{sn}(qx, q^{-1}). \tag{C.18}$$

Setting $k = q^{-1}$, so that $k < 1$, Eq. (C.17) can be written as

$$\theta(\bar{s}) = 2\arccos\left[\mathrm{sn}\left(k^{-1}(\bar{s}+\bar{s}_0), k\right)\right], \tag{C.19}$$

Now, using $\theta(0) = 0$, we get $\mathrm{sn}\left(k^{-1}\bar{s}_0, k\right) = 1$ and thus $k^{-1}\bar{s}_0 = (2n+1)K(k)$. Because sn is periodic, we can consider $n = 0$ and

$$\theta(\bar{s}) = 2\arccos\left[\mathrm{sn}\left(k^{-1}\bar{s} + K(k), k\right)\right]. \tag{C.20}$$

The parameter k is fixed by the BC $\theta(\bar{\ell}) = \pi/2 - \theta_Y$, where $\bar{\ell}$ is the unknown length of the interface. We also have

$$\theta'(\bar{s}) = 2k^{-1}\mathrm{dn}\left(k^{-1}\bar{s} + K(k), k\right), \tag{C.21}$$

where dn is another Jacobi elliptic function with the property $\mathrm{dn}(K(k), k) = (1-k^2)^{1/2}$. Therefore

$$\theta'(0) = 2k^{-1}(1-k^2)^{1/2}. \tag{C.22}$$

Finally, the energy is obtained by combining Eqs. (C.22) and (C.16c) and using the last BC in Eq. (C.16a):

$$\bar{U}_S = 2\bar{\delta}\left(1-k^{-2}\right), \tag{C.23a}$$

$$2\arccos\left[\mathrm{sn}\left(k^{-1}\bar{\ell} + K(k), k\right)\right] = \pi/2 - \theta_Y, \tag{C.23b}$$

$$\bar{\delta} = \int_0^{\bar{\ell}} \cos\theta(\bar{s})\, d\bar{s}. \tag{C.23c}$$

Knowing $\bar{\delta}$ and θ_Y together Eq. (C.20), Eqs. (C.23b) and (C.23c) fix $\bar{\ell}$ and k as well as the energy (C.23a).

Even if the nonlinear problem is solved rather easily, we do not obtain explicit expressions for the energy and capillary force. We thus follow another route and accept to lose some accuracy to obtain an explicit expression for the force.

Nonlinear problem: asymptotic solution. Here, we consider $\bar{\delta} \ll 1$, so that $\bar{\ell} \ll 1$, but θ_Y arbitrary (in contrast with the linear problem). We define a new spatial variable $r = \bar{s}/\bar{\ell}$ so that Eq. (C.16a) becomes

$$\frac{d^2\theta}{dr^2} = \epsilon \sin\theta(r), \quad \theta(0) = 0,\ \theta(1) = \pi/2 - \theta_Y, \tag{C.24}$$

where $\epsilon = \bar{\ell}^{\,2} \ll 1$. We now expand θ in power of ϵ:

$$\theta = \theta_0 + \epsilon\theta_1 + \epsilon^2\theta_2 + \cdots \tag{C.25}$$

To keep the calculation short and simple, we limit it to the leading order. It can be shown that the next order is quite negligible even for $\bar{\ell} = 0.5$. At the leading order, we get

$$\frac{d^2\theta_0}{dr^2} = 0, \quad \theta_0(0) = 0,\ \theta_0(1) = \pi/2 - \theta_Y. \tag{C.26}$$

The solution is

$$\theta_0(\bar{s}) = (\pi/2 - \theta_Y)\,\bar{s}/\bar{\ell}. \tag{C.27}$$

We thus get a solution with a constant curvature, i.e. an arc of circle. Using Eq. (C.16c), the energy reads

$$\bar{U}_S = -\frac{\bar{\delta}\,[\theta'(0)]^2}{2} = -\frac{\bar{\delta}\,(\pi/2 - \theta_Y)^2}{2\bar{\ell}^2}. \tag{C.28}$$

We need to relate $\bar{\ell}$ to $\bar{\delta}$ to get the final expression:

$$\bar{\delta} = \int_0^{\bar{\ell}} \cos\theta_0(\bar{s})\, d\bar{s} = \int_0^{\bar{\ell}} \cos\left(\frac{(\pi/2 - \theta_Y)\,\bar{s}}{\bar{\ell}}\right) d\bar{s}. \tag{C.29}$$

We thus obtain

$$\bar{\ell} = \bar{\delta}\,\frac{(\pi/2 - \theta_Y)}{\cos\theta_Y}. \tag{C.30}$$

Finally, using Eqs. (C.28) and (C.30), the energy reads

$$\bar{U}_S = -\frac{\cos^2\theta_Y}{2\bar{\delta}}. \tag{C.31}$$

Approximate expression for $\bar{U}_S$. In summary, we have obtained two simple expressions (C.14) and (C.31) for the energy,

$$\bar{U}_S = -\frac{\bar{\delta}\cot^2\theta_Y}{2\sinh^2\bar{\delta}}, \quad \theta_Y \simeq \frac{\pi}{2}, \tag{C.32a}$$

$$\bar{U}_S = -\frac{\cos^2\theta_Y}{2\bar{\delta}}, \quad \bar{\delta} \ll 1. \tag{C.32b}$$

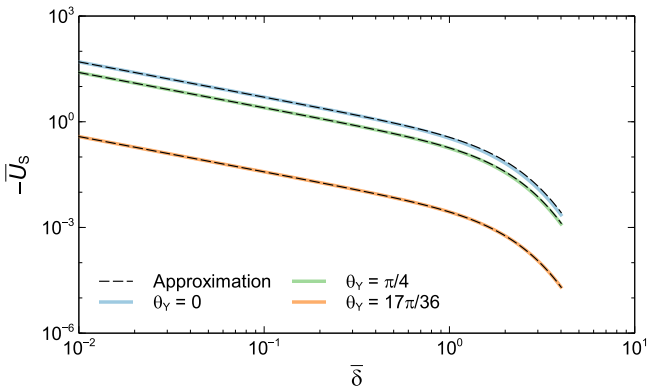

Fig. C.8. Evolution of the rescaled energy $\bar{U}_S = U_S/(\gamma\ell_c W)$ obtained by solving numerically Eqs. (C.23) as a function of the rescaled half distance between the lamellae $\bar{\delta} = \delta/\ell_c$ (solid curves). These numerical data agree well with the approximate expression (C.33) (dashed curves).

Since $\cot\theta_Y \simeq \cos\theta_Y$ when $\theta_Y \simeq \pi/2$, and $\bar{\delta}/\sinh^2\bar{\delta} \simeq 1/\bar{\delta}$ when $\bar{\delta} \ll 1$, we propose the following expression for the energy:

$$\frac{U_S}{\gamma\ell_c W} \equiv \bar{U}_S = -\frac{\bar{\delta}\cos^2\theta_Y}{2\sinh^2\bar{\delta}}. \tag{C.33}$$

Fig. C.8 shows that Eq. (C.33) agrees well with the energy obtained by solving numerically Eqs. (C.23).

The force is obtained from $\bar{F} = -\partial\bar{U}_S/\partial\bar{\delta}$:

$$\frac{F}{\gamma W} \equiv \bar{F}(\bar{\delta}) = -\frac{\cos^2\theta_Y}{2}\,\frac{[2\bar{\delta}\,\coth\bar{\delta} - 1]}{\sinh^2\bar{\delta}}, \tag{C.34}$$

where $\bar{\delta} = \delta/\ell_c$. In our experiments, $\delta \ll \ell_c$ and, in this limit, the expression of the force reduces to

$$F = -\frac{\gamma W}{2}\cos^2\theta_Y\,(\delta/\ell_c)^{-2}, \tag{C.35}$$

which coincide with Eq. (7b) of the main text.

Total energy

The total energy, U_L, of half the system is given by

$$\begin{aligned} U_L &= U_B + U_T + U_S, \\ &= \frac{B}{2}\int_0^L [w''(x)]^2\, dx + \frac{T}{2}\int_0^L [w'(x)]^2\, dx + U_S. \end{aligned} \tag{C.36}$$

Using the expression of w given by Eq. (4) of the main text and the expression (C.33) of U_S (with $\bar{\delta} = \bar{d}_L(1-A)$), we get

$$U_L(A) = \frac{BA^2d^2}{2L^3}\,\frac{\alpha^3}{\alpha - \tanh\alpha} - \frac{\gamma\ell_c W\cos^2\theta_Y\,[\bar{d}_L(1-A)]}{2\sinh^2[\bar{d}_L(1-A)]}. \tag{C.37}$$

Now, we define a rescaled energy

$$\bar{U}_L = \frac{U_L}{\beta}, \quad \beta = \frac{Bd^2}{L^3}\,\frac{\alpha^3}{\alpha - \tanh\alpha}, \tag{C.38}$$

so that

$$\bar{U}_L(A) = \frac{A^2}{2} - \frac{\Lambda_L(1-A)}{2\bar{d}_L\sinh^2[\bar{d}_L(1-A)]}. \tag{C.39}$$

In the limit $\bar{\delta} = \bar{d}_L(1-A) \ll 1$ (i.e. $\delta \ll \ell_c$), the energy reduces to

$$\bar{U}_L = \frac{A^2}{2} - \frac{\Lambda_L}{2\bar{d}_L^3(1-A)}, \tag{C.40}$$

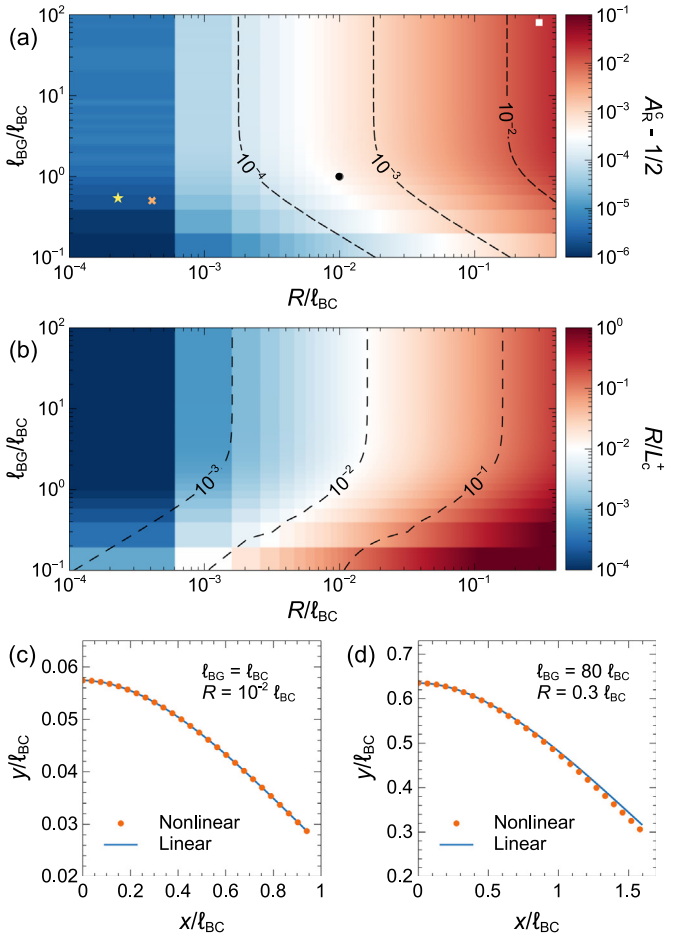

Fig. C.9. Evolution of $A_R^c - 1/2$ (a) and R/L_c^+ (b), computed with the nonlinear model Eqs. (D.1)–(D.5) for rods with $\theta_Y = 0$, as a function of ℓ_{BG}/ℓ_{BC} and R/ℓ_{BC}. The distance d between the rods is chosen to be the largest distance at which coalescence is possible. The yellow star and the orange cross refer respectively to the glass and PET fibers used in the experiments. The black disk and the white square correspond to the states shown in panels (c) and (d) respectively. Shape of one of the two rods at the limit of snapping for $\ell_{BG}/\ell_{BC} = 1$ and $R/\ell_{BC} = 10^{-2}$ (c) and for $\ell_{BG}/\ell_{BC} = 80$ and $R/\ell_{BC} = 0.3$ (d).

and we recover Eq. (9b) of the main text. The selected value of A is the one that minimize the energy which is obtained from the equation

$$\frac{\partial \bar{U}_L}{\partial A} = 0 = A - \frac{\Lambda_L}{2\bar{d}_L^3(1-A)^2}. \tag{C.41}$$

We recover Eq. (8b) of the main text.

Appendix D. Nonlinear beam model

The theory presented in this article is based on the linear beam equation. It may be extended to take into account potential large deformations of the structures. In this case, the elastica description of the slender structures can be used:

$$\frac{d^2\theta}{d\bar{s}^2} = \alpha^2 \sin\theta + \bar{F}\cos\theta, \quad \theta(0) = \theta'(1) = 0, \tag{D.1}$$

where $\bar{s} = s/L$ is the rescaled arclength, α is the dimensionless tension defined by Eq. (8d) and $\bar{F} = -FL^2/B$ is the dimensionless capillary force (7). Within this curvilinear framework, δ is given by:

$$\bar{\delta} \equiv \delta/L = \int_0^1 \sin\theta(\bar{s})\, d\bar{s} + \bar{d}, \tag{D.2}$$

where $\bar{d} = d/L$. Solving numerically Eq. (D.1) for given values of α and $\bar{F}$, yields the deflection $\bar{\delta}$ as a function of these two parameters; i.e. $\bar{\delta} = \bar{\delta}(\alpha, \bar{F})$. However, as the capillary force is a function of $\bar{\delta}$, we must impose that the value of $\bar{F}$ used to solve Eq. (D.1) is equal to the value of the capillary force (7) evaluated at $\bar{\delta}$ obtained from Eq. (D.2). In the following, we illustrate this consistency procedure for rods only. Assuming $\delta \gg R$ for simplicity, the consistency relation reads as

$$\bar{F}\,\bar{\delta}(\alpha, \bar{F}) = \frac{RL\cos^2\theta_Y}{2L_{BC}^2}. \tag{D.3}$$

The function $\bar{F}\,\bar{\delta}$ presents a maximum for an intermediate value of $\bar{F}$. Indeed, when $\bar{F} \to 0$, it vanishes because $\bar{\delta} \to \bar{d}$, and when $\bar{F}$ is sufficiently large, $\bar{\delta}$ tends to 0. In between these two zeros, $\bar{F}\,\bar{\delta}$ must pass through a maximum when $\bar{F}$ varies, that we note M. Therefore, the consistency relation (D.3) has a solution provided

$$M(\alpha(L)) \equiv \max_{\bar{F}}[\bar{F}\,\bar{\delta}(\alpha(L), \bar{F})] \geq \frac{RL\cos^2\theta_Y}{2L_{BC}^2}. \tag{D.4}$$

Following the same reasoning as in the linear case, no solution means that the only equilibrium state corresponds to contact between both rods. Hence, the critical dry length L_c^+ reads as

$$L_c^+ = \frac{2L_{BC}^2}{R\cos^2\theta_Y} M(\alpha(L_c^+)), \tag{D.5}$$

with $\alpha^2(L_c^+) = (L_c^+)^2/L_{BC}^2\cos\theta_Y + (L_c^+)^3/L_{BG}^3$. This relationship is transcendental and must be solved numerically to be compared to the linear theory. It appears to be a generalization of the linear model, see Eq. (8). Indeed, when $\theta \ll 1$, Eq. (D.1) reduces to

$$\frac{d^2\theta}{d\bar{s}^2} = \alpha^2\theta + \bar{F}, \quad \theta(0) = \theta'(1) = 0. \tag{D.6}$$

Solving this equation, we get,

$$\bar{\delta} = \bar{d} - \bar{F}\left(\frac{\alpha - \tanh\alpha}{\alpha^3}\right). \tag{D.7}$$

The maximum of the function $\bar{F}\,\bar{\delta}$ may then be easily computed and Eq. (D.5) is found to be identical to the equality between Eqs. (8) and (10), i.e. $\Lambda_R = \Lambda_R^c$.

Fig. C.9(a) shows $A_R^c - 1/2$ computed from the nonlinear model Eqs. (D.1)–(D.5). This quantity, which vanishes for a linear theory (see Eq. (10)), is a measure of the importance of the nonlinear effects which appear to be significant only when $\ell_{BG} \gtrsim 10\,\ell_{BC}$ and $R \gtrsim \ell_{BC}$. This region corresponds to very soft and small rods with a moderate aspect ratio. Indeed, using for example $\rho_s = 1000$ kg/m^3 and $\gamma = 0.021$ N/m, $\ell_{BG} = 10\,\ell_{BC}$ and $R = \ell_{BC}$ correspond to $E \simeq 2500$ Pa and $R \simeq 65$ μm. In addition, Fig. C.9(b) shows that in this region L_c^+ is only few times larger than R.

References

[1] B. Roman, J. Bico, Elasto-capillarity: deforming an elastic structure with a liquid droplet, J. Phys. Condens. Matter 22 (49) (2010) 493101, http://dx.doi.org/10.1088/0953-8984/22/49/493101.
[2] J. Bico, E. Reyssat, B. Roman, Elastocapillarity: when surface tension deforms elastic solids, Annu. Rev. Fluid Mech. 50 (2018) 629–659, http://dx.doi.org/10.1146/annurev-fluid-122316-050130.
[3] J. Bico, B. Roman, L. Moulin, A. Boudaoud, Elastocapillary coalescence in wet hair, Nature 432 (7018) (2004) 690, http://dx.doi.org/10.1038/432690a.
[4] A. Boudaoud, J. Bico, B. Roman, Elastocapillary coalescence: aggregation and fragmentation with a maximal size, Phys. Rev. E 76 (6) (2007) 060102, http://dx.doi.org/10.1103/PhysRevE.76.060102.

[5] C. Py, R. Bastien, J. Bico, B. Roman, A. Boudaoud, 3D aggregation of wet fibers, Europhys. Lett. 77 (4) (2007) 44005, http://dx.doi.org/10.1209/0295-5075/77/44005.
[6] T. Eisner, D.J. Aneshansley, Defense by foot adhesion in a beetle (*Hemisphaerota cyanea*), Proc. Natl. Acad. Sci. USA 97 (12) (2000) 6568–6573, http://dx.doi.org/10.1073/pnas.97.12.6568.
[7] O. Betza, G. Kölsch, The role of adhesion in prey capture and predator defence in arthropods, Arthropod Struct. Dev. 33 (1) (2004) 3–30, http://dx.doi.org/10.1016/j.asd.2003.10.002.
[8] W. Kim, T. Gilet, J.W. Bush, Optimal concentrations in nectar feeding, Proc. Natl. Acad. Sci. USA 108 (40) (2011) 16618–16621, http://dx.doi.org/10.1073/pnas.1108642108.
[9] W. Kim, J.W.M. Bush, Natural drinking strategies, J. Fluid Mech. 705 (2012) 7–25, http://dx.doi.org/10.1017/jfm.2012.122.
[10] W. Kim, F. Peaudecerf, M.W. Baldwin, J.W. Bush, The hummingbird's tongue: a self-assembling capillary syphon, Proc. R. Soc. B 279 (1749) (2012) 4990–4996, http://dx.doi.org/10.1098/rspb.2012.1837.
[11] A. Lechantre, A. Draux, H.-A.B. Hua, D. Michez, P. Damman, F. Brau, Essential role of papillae flexibility in nectar capture by bees, Proc. Natl. Acad. Sci. USA 118 (19) (2021) e2025513118, http://dx.doi.org/10.1073/pnas.2025513118.
[12] H. Elettro, S. Neukirch, F. Vollrath, A. Antkowiak, In-drop capillary spooling of spider capture thread inspires hybrid fibers with mixed solid–liquid mechanical properties, Proc. Natl. Acad. Sci. USA 113 (22) (2016) 6143–6147, http://dx.doi.org/10.1073/pnas.1602451113.
[13] T. Tanaka, M. Morigami, N. Atoda, Mechanism of resist pattern collapse during development process, Japan. J. Appl. Phys. 32 (12S) (1993) 6059–6064, http://dx.doi.org/10.1143/JJAP.32.6059.
[14] O. Raccurt, F. Tardif, F.A. d'Avitaya, T. Vareine, Influence of liquid surface tension on stiction of SOI MEMS, J. Micromech. Microeng. 14 (7) (2004) 1083, http://dx.doi.org/10.1088/0960-1317/14/7/031.
[15] J.-H. Jang, C.K. Ullal, M. Maldovan, T. Gorishnyy, S. Kooi, C. Koh, E.L. Thomas, 3D micro-and nanostructures via interference lithography, Adv. Funct. Mater. 17 (16) (2007) 3027–3041, http://dx.doi.org/10.1002/adfm.200700140.
[16] A.K. Geim, S. Dubonos, I. Grigorieva, K. Novoselov, A. Zhukov, S.Y. Shapoval, Microfabricated adhesive mimicking gecko foot-hair, Nature Mater. 2 (7) (2003) 461–463, http://dx.doi.org/10.1038/nmat917.
[17] M. Mastrangeli, S. Abbasi, C. Varel, C. Van Hoof, J.-P. Celis, K.F. Böhringer, Self-assembly from milli-to nanoscales: methods and applications, J. Micromech. Microeng. 19 (8) (2009) 083001, http://dx.doi.org/10.1088/0960-1317/19/8/083001.
[18] B. Pokroy, S.H. Kang, L. Mahadevan, J. Aizenberg, Self-organization of a mesoscale bristle into ordered, hierarchical helical assemblies, Science 323 (5911) (2009) 237–240, http://dx.doi.org/10.1126/science.1165607.
[19] M. De Volder, A.J. Hart, Engineering hierarchical nanostructures by elasto-capillary self-assembly, Angew. Chem. Int. Ed. 52 (9) (2013) 2412–2425, http://dx.doi.org/10.1002/anie.201205944.
[20] J. Van Honschoten, J.W. Berenschot, T. Ondarçuhu, R.G. Sanders, J. Sundaram, M. Elwenspoek, N.R. Tas, Elastocapillary fabrication of three-dimensional microstructures, Appl. Phys. Lett. 97 (1) (2010) 014103, http://dx.doi.org/10.1063/1.3462302.
[21] X. Liu, M. Wei, Q. Wang, Y. Tian, J. Han, H. Gu, H. Ding, Q. Chen, K. Zhou, Z. Gu, Capillary-force-driven self-assembly of 4D-printed microstructures, Adv. Mater. 33 (22) (2021) 2100332, http://dx.doi.org/10.1002/adma.202100332.
[22] Z. Wei, T.M. Schneider, J. Kim, H.-Y. Kim, J. Aizenberg, L. Mahadevan, Elastocapillary coalescence of plates and pillars, Proc. R. Soc. Lond. Ser. A Math. Phys. Eng. Sci. 471 (2175) (2015) 20140593, http://dx.doi.org/10.1098/rspa.2014.0593.
[23] A. Hadjittofis, J.R. Lister, K. Singh, D. Vella, Evaporation effects in elasto-capillary aggregation, J. Fluid Mech. 792 (2016) 168–185, http://dx.doi.org/10.1017/jfm.2016.80.
[24] C. Duprat, J.M. Aristoff, H.A. Stone, Dynamics of elastocapillary rise, J. Fluid Mech. 679 (2011) 641–654, http://dx.doi.org/10.1017/jfm.2011.173.
[25] J.M. Aristoff, C. Duprat, H.A. Stone, Elastocapillary imbibition, Int. J. Non-Linear Mech. 46 (4) (2011) 648–656, http://dx.doi.org/10.1016/j.ijnonlinmec.2010.09.001.
[26] A.T. Bradley, F. Box, I.J. Hewitt, D. Vella, Wettability-independent droplet transport by Bendotaxis, Phys. Rev. Lett. 122 (7) (2019) 074503, http://dx.doi.org/10.1103/PhysRevLett.122.074503.
[27] M.M. Nicolson, The interaction between floating particles, in: Mathematical Proceedings of the Cambridge Philosophical Society, Vol. 45, Cambridge University Press, 1949, pp. 288–295, http://dx.doi.org/10.1017/S0305004100024841.
[28] P. Kralchevsky, V. Paunov, I. Ivanov, K. Nagayama, Capillary meniscus interaction between colloidal particles attached to a liquid-fluid interface, J. Colloid Interface Sci. 151 (1) (1992) 79–94, http://dx.doi.org/10.1016/0021-9797(92)90239-I.
[29] P.A. Kralchevsky, V.N. Paunov, N.D. Denkov, I.B. Ivanov, K. Nagayama, Energetical and force approaches to the capillary interactions between particles attached to a liquid-fluid interface, J. Colloid Interface Sci. 155 (2) (1993) 420–437, http://dx.doi.org/10.1006/jcis.1993.1056.
[30] P.A. Kralchevsky, K. Nagayama, Capillary forces between colloidal particles, Langmuir 10 (1) (1994) 23–36, http://dx.doi.org/10.1021/la00013a004.
[31] C.D. Dushkin, P.A. Kralchevsky, V.N. Paunov, H. Yoshimura, K. Nagayama, Torsion balance for measurement of capillary immersion forces, Langmuir 12 (3) (1996) 641–651, http://dx.doi.org/10.1021/la950560p.
[32] A. Kralchevsky, K. Nagayama, Particles at Fluids Interfaces and Membranes: Attachment of Colloid Particles and Proteins to Interfaces and Formation of Two-Dimensional Arrays, in: Studies in Interface Science, vol. 10, Elsevier, Amsterdam, 1988.
[33] D. Vella, L. Mahadevan, The "cheerios effect", Amer. J. Phys. 73 (9) (2005) 817–825, http://dx.doi.org/10.1119/1.1898523.
[34] H. Cooray, P. Cicuta, D. Vella, The capillary interaction between two vertical cylinders, J. Condens. Matter Phys. 24 (28) (2012) 284104, http://dx.doi.org/10.1088/0953-8984/24/28/284104.
[35] I. Ho, G. Pucci, D.M. Harris, Direct measurement of capillary attraction between floating disks, Phys. Rev. Lett. 123 (25) (2019) 254502, http://dx.doi.org/10.1103/PhysRevLett.123.254502.
[36] M. Poty, N. Vandewalle, Equilibrium distances for the capillary interaction between floating objects, Soft Matter 17 (2021) 6718–6727, http://dx.doi.org/10.1039/D1SM00447F.
[37] L. Botto, E.P. Lewandowski, M. Cavallaro, K.J. Stebe, Capillary interactions between anisotropic particles, Soft Matter 8 (39) (2012) 9957–9971, http://dx.doi.org/10.1039/C2SM25929J.
[38] R. McGorty, J. Fung, D. Kaz, V.N. Manoharan, Colloidal self-assembly at an interface, Mater. Today 13 (6) (2010) 34–42, http://dx.doi.org/10.1016/S1369-7021(10)70107-3.
[39] D. Shin, S. Tawfick, Polymorphic elastocapillarity: Kinetically reconfigurable self-assembly of hair bundles by varying the drain rate, Langmuir 34 (21) (2018) 6231–6236, http://dx.doi.org/10.1021/acs.langmuir.8b00593.
[40] L. Kovanko, S. Tawfick, Capillary-induced hair twist, Langmuir 35 (41) (2019) 13421–13426, http://dx.doi.org/10.1021/acs.langmuir.9b01441.
[41] J. Ha, Y.S. Kim, K. Jiang, R. Siu, S. Tawfick, Hydrodynamic elastocapillary morphing of hair bundles, Phys. Rev. Lett. 125 (25) (2020) 254503, http://dx.doi.org/10.1103/PhysRevLett.125.254503.
[42] H. Yang, J. Wu, S. Yan, Effects of erectable glossal hairs on a honeybee's nectar-drinking strategy, Appl. Phys. Lett. 104 (26) (2014) 263701, http://dx.doi.org/10.1063/1.4886115.
[43] C.J. Harper, S.M. Swartz, E.L. Brainerd, Specialized bat tongue is a hemodynamic nectar mop, Proc. Natl. Acad. Sci. USA 110 (22) (2013) 8852–8857, http://dx.doi.org/10.1073/pnas.1222726110.
[44] P.-G. de Gennes, F. Brochard-Wyart, D. Quéré, Capillarity and Wetting Phenomena: Drops, Bubbles, Pearls, Waves, Springer-Verlag, New-York, 2004.
[45] D. Vella, A. Boudaoud, M. Adda-Bedia, Statics and inertial dynamics of a ruck in a rug, Phys. Rev. Lett. 103 (17) (2009) 174301, http://dx.doi.org/10.1103/PhysRevLett.103.174301.
[46] H.-Y. Kim, L. Mahadevan, Capillary rise between elastic sheets, J. Fluid Mech. 548 (2006) 141–150, http://dx.doi.org/10.1017/S0022112005007718.
[47] C. Py, P. Reverdy, L. Doppler, J. Bico, B. Roman, C.N. Baroud, Capillary origami: spontaneous wrapping of a droplet with an elastic sheet, Phys. Rev. Lett. 98 (15) (2007) 156103, http://dx.doi.org/10.1103/PhysRevLett.98.156103.
[48] V. Romero, M. Ly, A.-H. Rasheed, R. Charrondière, A. Lazarus, S. Neukirch, F. Bertails-Descoubes, Physical validation of simulators in Computer Graphics: A new framework dedicated to slender elastic structures and frictional contact, ACM Trans. Graph. 40 (4) (2021) 66, http://dx.doi.org/10.1145/3450626.3459931.
[49] F.W.J. Olver, D.W. Lozier, R.F. Boisvert, C.W. Clark (Eds.), NIST Handbook of Mathematical Functions, Cambridge University Press, Cambridge, 2010.